REGULAR PAPER

Ultrasonic measurement of carotid luminal surface roughness with removal of axial displacement caused by blood pulsation

Japanese Journal of Applied Physics **62**, SJ1042 (2023) **REGULAR PAPER**
https://doi.org/**10.35848/1347-4065/acc07a**

Ultrasonic measurement of carotid luminal surface roughness with removal of axial displacement caused by blood pulsation

Ryota Yamane[1], Shohei Mori[2*], Mototaka Arakawa[1,2], Jens E. Wilhjelm[3], and Hiroshi Kanai[1,2]

[1]*Graduate School of Biomedical Engineering, Tohoku University, Sendai, Miyagi 980-8579, Japan*
[2]*Graduate School of Engineering, Tohoku University, Sendai, Miyagi 980-8579, Japan*
[3]*Department of Health Technology, Technical University of Denmark, Kgs. Lyngby, Denmark*

[*]E-mail: mori@tohoku.ac.jp

Received November 15, 2022; revised February 3, 2023; accepted March 1, 2023; published online April 3, 2023

For early diagnosis of atherosclerosis, we have developed a method to measure the initial minute surface roughness utilizing the natural longitudinal displacement of the intima-media-complex (IMC) on the carotid artery caused by pulsation. However, the IMC displaces not only in the longitudinal direction but also in the axial direction due to the pulsation. In the present paper, we proposed a novel method to remove the pulsation component by spatially convolving a high-pass filter with the measured depths of IMC in the longitudinal direction. The proposed method was validated by a phantom experiment, and the surface roughness with ten saw teeth was correctly measured. Next, the surface roughness of the carotid artery wall was measured for two healthy volunteers. The proposed method reduced the variation of measured surface roughness among beams compared to the previous method. © 2023 The Japan Society of Applied Physics

1. Introduction

Cardiovascular diseases such as strokes and myocardial infarctions are the leading causes of death worldwide.[1)] These diseases are primarily caused by atherosclerosis.[2)] Thus, diagnosis of atherosclerosis in the early stage would be very beneficial.

Several techniques for this end have been applied. Pulse wave velocity (PWV), an indicator of arterial wall stiffness, has been used to diagnose atherosclerosis.[3–5)] An intima-media complex (IMC) thickness (IMT) of the carotid artery wall, measured by ultrasound, has also been used for the diagnosis of atherosclerosis[6)] because the hypertrophy of the arterial wall is associated with future atherosclerosis.[7)]

In experiments on the blood vessels of rabbits exposed to high blood pressure for seven days, it was considered that the luminal surface on the arterial wall became rough at approximately 10 micrometers.[8)] The appearance of surface roughness is considered the first step in arterial hypertrophy caused by flow and shear stress,[8–10)] and its noninvasive evaluation contributes to the early detection of atherosclerosis. Thus, methods to ultrasonically measure surface roughness have been studied.[11–22)] It has been reported that this roughness is caused by an increase in endothelial cells and damage to the internal elastic lamina.[8)] Since there is no significant difference in cell size between humans and rabbits,[23,24)] the height of the surface roughness in human may be the same order with that of rabbits.

An ultrasound B-mode image is normally constructed using a constant assumed sound speed; however, there are regions of non-uniform sound-speed between the probe and the anterior wall of the carotid artery. If the thickness of the region of non-uniform sound-speed is 8 mm and the assumed sound speed is 1540 m s^{-1}, then a difference of 1% in the sound speed causes a measured depth error of approximately 80 μm. Since the measured depth error varies with the beam position due to inhomogeneities in sound speed, it is difficult to measure the minute surface roughness only from the conventional B-mode image.

In previous studies, we proposed a method to measure the minute surface roughness using a single ultrasound beam by utilizing the naturally occurring longitudinal displacement of IMC caused by pulsation. The method can measure the surface roughness without being affected by the region of non-uniform sound-speed by combining the naturally occurring longitudinal displacement caused by pulsation and the axial displacement caused by the difference in the surface roughness in the longitudinal direction, described in detail in the methods section. However, the IMC displaces not only in the longitudinal direction but also in the axial direction by the pulsation, and the measured axial displacement includes not only the surface roughness component but also the axial displacement of the IMC due to pulsation (pulsation component). Therefore, the pulsation component should be removed. Previously, this pulsation component was removed by assuming that it is the same in all longitudinal positions.[19–21)] However, the pulsation component slightly differs by the longitudinal position[25–28)], and its effect on the estimate of the surface roughness is not negligible. The influence on inclination angle change between IMC and the probe surface by pulsation during the surface roughness measurement is discussed in result section. This study aims to diagnose atherosclerosis at a very early stage where the plaque has not yet formed; therefore, it is assumed that there is no sound-speed difference in the longitudinal direction of the arterial wall itself.

Thus, in the present study, we propose a novel method to remove the axial displacement due to pulsation by introducing a spatial high-pass filter (HPF) along the longitudinal direction. The proposed method is validated by the phantom experiment.[29)] Finally, the luminal surface roughness of the carotid artery wall for two healthy young volunteers was measured as well.

2. Methods

2.1. Surface roughness estimation using natural longitudinal movement of carotid arterial wall

Consider the measurement situation in Fig. 1(a). The global coordinate system is defined by (x, z) with the origin (0, 0) at the interface between the transducer composed of an array of piezoelectric elements and skin, and at the center lateral position of beam 0. The transducer creates M beams

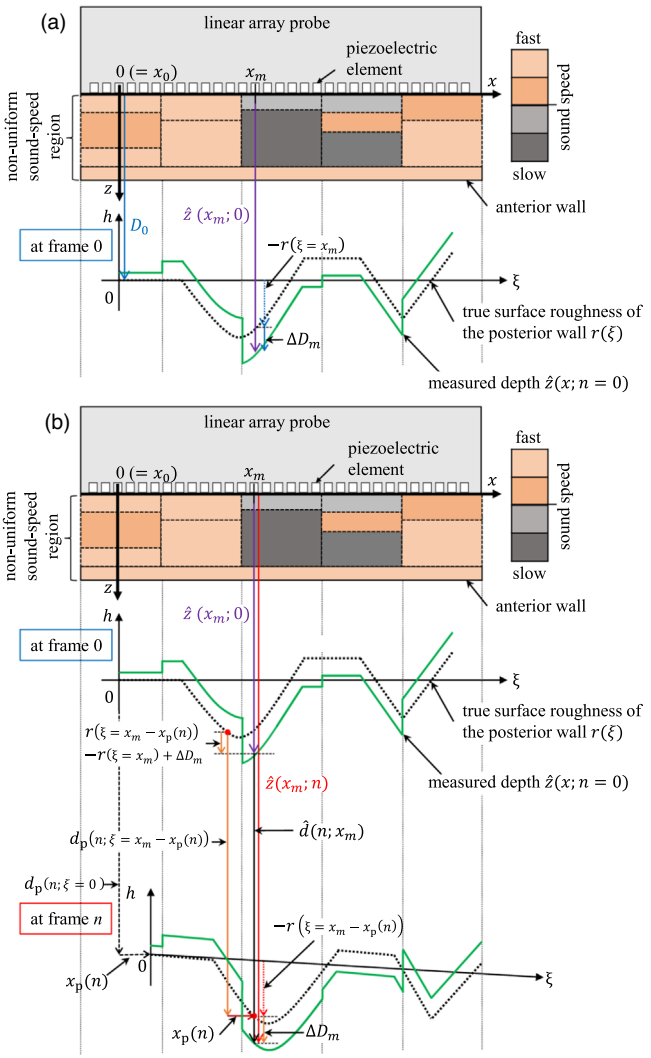

Fig. 1. (Color online) Schematic of the surface roughness measurement (a) at initial frame and (b) at frame n.

$[0; M-1]$ and N image frames $[0; N-1]$. The lateral position of the center of the beam m is defined by x_m.

The interface between blood and intima of the posterior wall is described by the surface profile $r(\xi)$ (black dotted line), which we would like to estimate, in the coordinate system (ξ, h) set on the luminal surface of the IMC. At frame 0, the origin of the ξ axis is located at $x = 0$ in the global coordinate system, i.e. the lateral position of the center of beam 0. The depth from the probe surface to the surface profile $r(\xi = 0)$ at beam 0 at frame 0 is defined by a baseline of the surface profile, D_0. At this time, the position of the surface profile at beam 0 at frame 0 in the global coordinate system (x, z) is $(x = 0, z = D_0)$ as shown in Fig. 1(a).

Since the surface profile $r(\xi)$ moves in the global coordinate system (x, z) by pulsation, a single scan line can measure a part of the posterior wall surface that moves across the beam. Since the region of non-uniform sound-speed does not move and the single beam passes through the same region during the measurement, surface roughness measured by the single beam is not affected by the region of non-uniform sound-speed, as clarified in our previous methods.[19–22)]

At the initial frame 0, the depth of IMC, $\hat{z}(x_m; 0)$ at x_m [purple arrow in Fig. 1(a)], is determined by thresholding the enveloped RF signal. As shown by the purple arrow in Fig. 1(a), $\hat{z}(x_m; 0)$ is divided into the following three components as shown by the blue arrows:

$$\hat{z}(x_m; 0) = D_0 + \Delta D_m - r(\xi = x_m), \tag{1}$$

where ΔD_m is the height shift caused by the region of non-uniform sound-speed between the probe surface and anterior wall. The negative sign for $r(\xi = x_m)$ is due to the difference of the direction of z in the global coordinate system and that of h in the coordinate system set on the luminal surface of IMC. Here, the surface roughness $r(\xi = 0)$ at $\xi = 0$ is defined as 0 as shown in Fig. 1(a); therefore

$$\hat{z}(0; 0) = D_0 + \Delta D_0. \tag{2}$$

From frame $(n-1)$ to frame n, the surface profile $r(\xi)$ displaces by the 2D vector $(\Delta x_p(n),\ \Delta d_p(n; \xi))$, where the displacement is naturally caused by the pulsation of the wall, that is, the movements in the longitudinal and axial directions. The total longitudinal displacement $x_p(n)$ and the total axial displacement $d_p(n; \xi)$ of the wall from the initial frame 0 to frame n are given by the following accumulations

$$x_p(n) = \sum_{k=0}^{n} \Delta x_p(k), \tag{3}$$

$$d_p(n; \xi) = \sum_{k=0}^{n} \Delta d_p(k; \xi). \tag{4}$$

As with previous studies,[19–22)] the longitudinal displacement $x_p(n)$ due to pulsation is assumed to be the same in the measurement region (its width was 9.15 mm in this study) and is estimated using the block-matching method[30,31)] by applying the reconstructive interpolation[32)] to the correlation values between the envelope of RF signals of consecutive frames.

Let $\hat{z}(x_m; n)$ denotes the measured depth of the surface profile by beam m at frame n. This is the red arrow in Fig. 1(b) and is given by

$$\hat{z}(x_m; n) = \hat{z}(x_m; 0) + \sum_{k=0}^{n} \widehat{\Delta d}(k; x_m), \tag{5}$$

where $\widehat{\Delta d}(n; x_m)$ is the axial displacement from frames $n-1$ to n measured by applying the phased-tracking method to the RF signals.[33–35)] As shown by the orange arrows in Fig. 1(b), the total axial displacement $\hat{d}(n; x_m)$ of the wall from frames 0 to n is divided as

$$\begin{aligned}\hat{d}(n; x_m) &= \sum_{k=0}^{n} \widehat{\Delta d}(k; x_m). \\ &= d_p(n; \xi = x_m - x_p(n)) \\ &\quad - \{r(\xi = x_m - x_p(n)) - r(\xi = x_m) + \Delta D_m\} \\ &\quad + \Delta D_m \\ &= d_p(n; \xi = x_m - x_p(n)) \\ &\quad - \{r(\xi = x_m - x_p(n)) - r(\xi = x_m)\}.\end{aligned} \tag{6}$$

The first term $d_p(n; \xi = x_m - x_p(n))$ of the last equation shows the axial displacement of the wall at the position $\xi = x_m - x_p(n)$ caused by the pulsation from frames 0 to n. The second term shows the difference in roughness between $r(\xi = x_m - x_p(n))$ measured by beam m at frame n and

$r(\xi = x_m)$ measured by beam m at frame 0, whose difference is caused by the longitudinal displacement $x_\mathrm{p}(n)$ of IMC.

By substituting Eqs. (1) and (6) into Eq. (5), the measured depth of IMC at frame n, $\hat{z}(x_m; n)$, is divided into four components as

$$\hat{z}(x_m; n) = D_0 - r(\xi = x_m - x_\mathrm{p}(n)) + d_\mathrm{p}(n; \xi = x_m - x_\mathrm{p}(n)) + \Delta D_m. \tag{7}$$

Thus, it is found that the measured depth of the surface of IMC, $\hat{z}(x_m; n)$, is composed of the base depth D_0 from the probe to the surface of IMC at the initial frame at $\xi = 0$, the true surface profile $r(\xi = x_m - x_\mathrm{p}(n))$ at the longitudinal position of $\xi = x_m - x_\mathrm{p}(n)$, the axial displacement of the wall, $d_\mathrm{p}(n; \xi = x_m - x_\mathrm{p}(n))$, caused by pulsation, and the height shift ΔD_m due to the regions of non-uniform sound-speed. It is necessary to remove the three components $d_\mathrm{p}(n; \xi)$, ΔD_m, and D_0 from $\hat{z}(x_m; n)$ to estimate the surface roughness $r(\xi)$, as will be described below.

2.2. Removal of total axial displacement $d_\mathrm{p}(n; \xi)$ caused by pulsation

The axial displacement caused by pulsation, $d_\mathrm{p}(n; \xi)$, is removed as follows. Since the typical PWVs in humans are approximately 5–10 m s^{-1} [36] and the dominant frequency of the pulse wave is less than 20 Hz, the wavelength at 20 Hz is approximately 25–50 cm. Therefore, the spatial frequency along the longitudinal direction of the axial displacement caused by pulsation can be assumed to be much lower than that of surface roughness. Thus, the axial displacement caused by pulsation, $d_\mathrm{p}(n; \xi)$, is removed by applying the spatial convolution of the HPF $g(x)$ to the measured depth of the IMC, $\hat{z}(x_m; n)$, obtained by Eq. (5), along the longitudinal direction. The resultant $\hat{z}_\mathrm{HPF}(x_m; n)$ is given by

$$\begin{aligned}
&\hat{z}_\mathrm{HPF}(x_m; n) \\
&= \sum_{i=-W}^{W} g(\delta x \cdot i) \cdot \hat{z}(x_{m-i}; n) \\
&= \sum_{i=-W}^{W} g(\delta x \cdot i) \\
&\{D_0 - r(\xi = x_{m-i} - x_\mathrm{p}(n)) + d_\mathrm{p}(n; \xi = x_{m-i} - x_\mathrm{p}(n)) + \Delta D_{m-i}\} \\
&= \sum_{i=-W}^{W} g(\delta x \cdot i)\{D_0 + d_\mathrm{p}(n; \xi = x_{m-i} - x_\mathrm{p}(n))\} \\
&+ \sum_{i=-W}^{W} g(\delta x \cdot i)\{\Delta D_{m-i} - r(\xi = x_{m-i} - x_\mathrm{p}(n))\},
\end{aligned} \tag{8}$$

where $2W + 1$ denotes the window width of the HPF and δx is the beam spacing.

Figure 2 shows the measured depth $\hat{z}(x_m; n)$ and the four components included in the measured depth $\hat{z}(x_m; n)$ together with the results of the convolutions with the HPF. As shown in Fig. 2, the depth D_0 from the probe to the base of the surface profile is a constant, and the axial displacement caused by pulsation, $d_\mathrm{p}(n; \xi)$, is assumed to include spatially lower frequency components. Thus, these components can be removed by the HPF $g(x)$. That is, the first term in the last equation of Eq. (8) becomes zero by properly setting the cutoff frequency. The second term, which is composed of the surface roughness $r(\xi)$ and the height shift ΔD_m due to the regions of non-uniform sound-speed, remains after applying the HPF. The resultant components, denoted by $r_{\mathrm{HPF},m}(\xi)$ and $\Delta D_{\mathrm{HPF},m}$, are given by Eqs. (9) and (10), respectively.

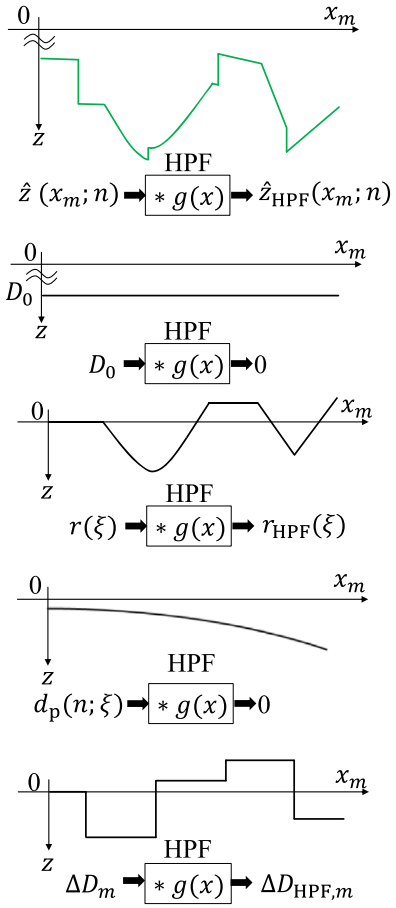

Fig. 2. (Color online) HPF for removing axial displacements caused by pulsation. By applying HPF, components of pulsation $d_\mathrm{p}(n; \xi)$ and baseline of surface profile, D_0, are removed, while components of the surface roughness $r_\mathrm{HPF}(\xi)$ and height shift due to region non-uniform sound-speed, ΔD_HPF, pass through the HPF.

$$\begin{aligned}
&r_{\mathrm{HPF},m}(\xi = x_m - x_\mathrm{p}(n)) \\
&= \sum_{i=-W}^{W} g(\delta x \cdot i) \cdot r(\xi = x_{m-i} - x_\mathrm{p}(n)),
\end{aligned} \tag{9}$$

$$\Delta D_{\mathrm{HPF},m} = \sum_{i=-W}^{W} g(\delta x \cdot i) \Delta D_{m-i}. \tag{10}$$

Thus, by applying the HPF, the remaining displacement $\hat{z}_\mathrm{HPF}(x_m; n)$ has the following two components as

$$\hat{z}_\mathrm{HPF}(x_m; n) \approx -r_{\mathrm{HPF},m}(\xi = x_m - x_\mathrm{p}(n)) + \Delta D_{\mathrm{HPF},m}. \tag{11}$$

2.3. Removal of height shift $\Delta D_{\mathrm{HPF},m}$ caused by region of non-uniform sound-speed

Though the axial displacement of IMC due to pulsation, $d_\mathrm{p}(n; \xi)$, is removed by a HPF, the resultant $\hat{z}_\mathrm{HPF}(x_m; n)$ still contains the height-shift component $\Delta D_{\mathrm{HPF},m}$ caused by the region of non-uniform sound-speed. The height-shift component $\Delta D_{\mathrm{HPF},m}$ is removed by the following procedure.

The resultant measured depth $\hat{z}_\mathrm{HPF}(x_m; n)$, defined in the global coordinate system $(x,\ z)$, is converted into the surface

profile $\hat{h}_m(\xi)$ measured with the beam m in the coordinate system (ξ, h) defined on the artery wall as follows:

$$\hat{h}_m(\xi = x_m - x_\mathrm{p}(n)) = \hat{z}_\mathrm{HPF}(x_m; n) \approx -r_{\mathrm{HPF},m}(\xi = x_m - x_\mathrm{p}(n)) + \Delta D_{\mathrm{HPF},m}. \quad (12)$$

Figure 3 shows the surface profile $\hat{h}_{m-1}(\xi)$ and $\hat{h}_m(\xi)$ measured with the beams $m-1$ and m in the coordinate system (ξ, h). As shown in Eq. (12) and in Fig. 3, $\hat{h}_m(\xi)$ contains the height-shift component, $\Delta D_{\mathrm{HPF},m}$, in addition to the roughness $r_{\mathrm{HPF},m}(\xi)$.

The height shift ΔD_m obtained before applying the HPF is determined by the sound speed distribution in the region of non-uniform sound-speed. Therefore, both ΔD_m of Eq. (1) and $\Delta D_{\mathrm{HPF},m}$ of Eq. (10) do not change by frame n. Thus, for the surface profile measured by beam m, $\hat{h}_m(\xi = x_m - x_\mathrm{p}(n))$, the component $\Delta D_{\mathrm{HPF},m}$ is constant regardless of $\xi = x_m - x_\mathrm{p}(n)$, as shown in Fig. 3.

The longitudinal measurement ranges of $\hat{h}_{m-1}(\xi)$ and $\hat{h}_m(\xi)$ partly overlap because the typical longitudinal displacement of the IMC during one heartbeat is approximately 1 mm[19] and much larger than the beam spacing δx (150 m in this study). In the overlapped measurement range, only the height-shift components $\Delta D_{\mathrm{HPF},m-1}$ and $\Delta D_{\mathrm{HPF},m}$ are different between beams, as shown in Fig. 3.

Therefore, the height shift $\Delta D_{\mathrm{HPF},m}$ can be estimated by minimizing the root mean squared difference (RMSD) between $\hat{h}_{m-1}(\xi)$ and $\hat{h}_m(\xi)$ in the overlapped measurement range by the following procedure.

The spatial sampling position ξ of the surface profile $\hat{h}_m(\xi = x_m - x_\mathrm{p}(n))$ measured by beam m is determined by the initial beam position x_m and the longitudinal displacement caused by pulsation, $x_\mathrm{p}(n)$. Because the longitudinal instantaneous displacement of IMC, $x_\mathrm{p}(n) - x_\mathrm{p}(n-1)$, differs by frame n, the spatial sampling position $\xi = x_m - x_\mathrm{p}(n)$ is not evenly spaced. In addition, the initial sampling position $\xi = x_m$ of the surface profile $\hat{h}_m(\xi = x_m)$ at frame 0 differs by beam m. Thus, the RMSD between $\hat{h}_m(\xi)$ and $\hat{h}_{m-1}(\xi)$ cannot be evaluated at the same longitudinal position. Therefore, the surface profile $\hat{h}_m(\xi = x_m - x_\mathrm{p}(n))$ is interpolated to obtain the surface profile $\hat{h}_{\mathrm{in},m}(\xi)$ at the constant sampling intervals of 1 μm for the evaluation of the RMSD at the same longitudinal position, as shown in Fig. 3.

For the roughness measurement, only the relative difference $\widehat{\Delta D}_{\mathrm{HPF},m} - \widehat{\Delta D}_{\mathrm{HPF},m-1}$ should be estimated, where $\widehat{\Delta D}_{\mathrm{HPF},0}$ at initial beam 0 is set to 0. Thereafter, the height shift $\Delta D_{\mathrm{HPF},m}$ is estimated by minimizing the following RMSD ε_m for the spatially interpolated surface profile $\hat{h}_{\mathrm{in},m}(\xi)$ in the overlapped measurement range as

$$\widehat{\Delta D}_{\mathrm{HPF},m} = \begin{cases} 0, & m = 0 \\ \arg\min\limits_{\Delta D_{\mathrm{HPF},m}} \varepsilon_m, & m > 0, \end{cases} \quad (13)$$

$$\varepsilon_m = \sqrt{\frac{1}{|\, x_{m-1} - (x_m - x_\mathrm{p}(N-1))\,|} \sum_{\xi = x_m - x_\mathrm{p}(N-1)}^{x_{m-1}} \{\hat{h}_{\mathrm{in},m}(\xi) - \hat{h}_{\mathrm{in},m-1}(\xi) + \widehat{\Delta D}_{\mathrm{HPF},m-1}\}^2} = \sqrt{\frac{1}{|\, x_{m-1} - (x_m - x_\mathrm{p}(N-1))\,|} \sum_{\xi = x_m - x_\mathrm{p}(N-1)}^{x_{m-1}} \{\widehat{\Delta D}_{\mathrm{HPF},m} - \widehat{\Delta D}_{\mathrm{HPF},m-1} + \widehat{\Delta D}_{\mathrm{HPF},m-1}\}^2}, \quad (14)$$

where N is the total number of frames used for the surface roughness measurement.

Thus, the surface roughness $\hat{r}_{\mathrm{HPF},m}(\xi)$ measured by beam m is obtained by removing the estimated height shift $\widehat{\Delta D}_{\mathrm{HPF},m}$ from $\hat{h}_{\mathrm{in},m}(\xi)$ as

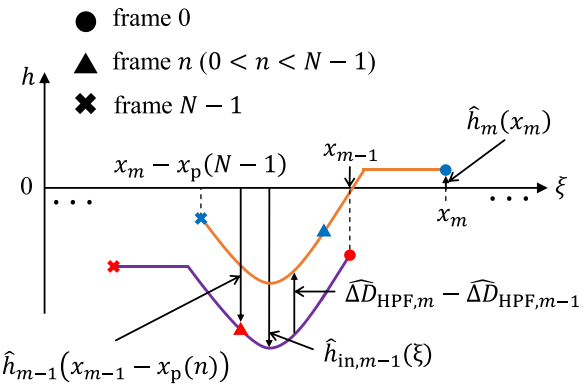

Fig. 3. (Color online) Measured surface profile $\hat{h}_m(\xi)$ after removing the axial displacement $d_\mathrm{p}(n;\, \xi)$ due to pulsation using the HPF, which still contains the height shift component, $\widehat{\Delta D}_{\mathrm{HPF},m}$, caused by the non-uniform sound speed in addition to the surface roughness $r_\mathrm{HPF}(\xi)$.

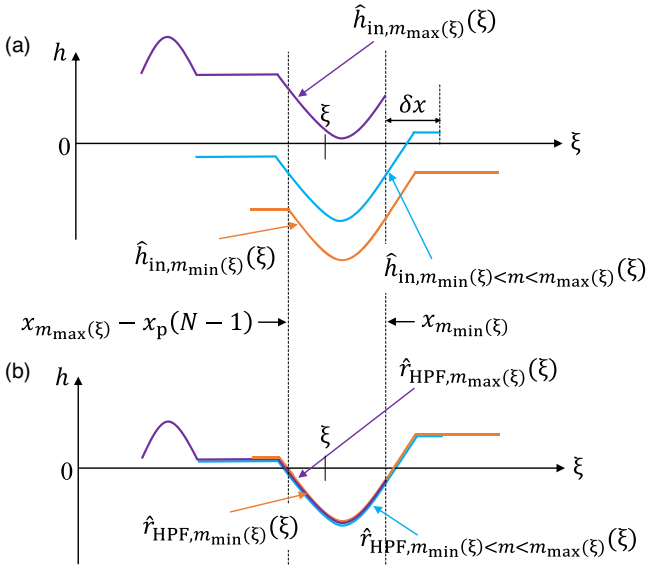

Fig. 4. (Color online) (a) Interpolated surface profile $\hat{h}_{\mathrm{in},m}(\xi)$ and (b) Surface roughness $\hat{r}_{\mathrm{HPF},m}(\xi)$ obtained by removing the height shift $\widehat{\Delta D}_{\mathrm{HPF},m}$ from the interpolated surface profile $\hat{h}_{\mathrm{in},m}(\xi)$.

$$\hat{r}_{\mathrm{HPF},m}(\xi) = \hat{h}_{\mathrm{in},m}(\xi) - \widehat{\Delta D}_{\mathrm{HPF},m}. \tag{15}$$

Figures 4(a) and 4(b) show the interpolated surface profiles $\hat{h}_{\mathrm{in},m}(\xi)$ and the surface roughnesses $\hat{r}_{\mathrm{HPF},m}(\xi)$ measured by beam m. Finally, the surface roughness $\hat{r}_{\mathrm{HPF}}(\xi)$ is obtained by averaging $\hat{r}_{\mathrm{HPF},m}(\xi)$ for multiple beams that measure the surface roughness for the same longitudinal position ξ, as shown in Fig. 4(b) as follows:

$$\hat{r}_{\mathrm{HPF}}(\xi) = \frac{1}{m_{\max}(\xi) - m_{\min}(\xi) + 1} \sum_{m=m_{\min}(\xi)}^{m_{\max}(\xi)} \hat{r}_{\mathrm{HPF},m}(\xi), \tag{16}$$

where

$$m_{\max}(\xi) = \max_{0 \le m \le \mathrm{M}-1} \left[\arg_m \{x_m - x_{\mathrm{p}}(n) < \xi\} \right], \tag{17}$$

$$m_{\min}(\xi) = \min_{0 \le m \le \mathrm{M}-1} \left[\arg_m \{x_m > \xi\} \right]. \tag{18}$$

2.4. Basic experiments using silicone phantom

Figure 5 shows the configuration of the basic experiment. We used a silicone phantom that had ten saw teeth with 10 μm height and 500 μm interval on the surface, that is, the spatial frequency of the surface roughness is 2 mm^{-1}. This phantom had the same saw teeth surface in the y direction as in Fig. 5. The reference surface profile of the phantom was measured using a laser displacement meter (LT9010; Keyence, Osaka, Japan). For simulating the blood vessel pulsation, the phantom was translated 1.0 mm at a speed of 1.4 mm s^{-1} in the longitudinal direction concurrently with a translation of 0.5 mm at a speed of 0.7 mm s^{-1} in the axial direction by an automated stage (ALD-906-E1P and ALZ-906-E1P; Chuo Precision Industrial, Tokyo, Japan). An ultrasound diagnostic apparatus (ProSound F75; Hitachi Aloka, Tokyo, Japan) with a linear array probe (UST-5415; Hitachi Aloka, Tokyo, Japan) was used for the ultrasonic measurements. The transmitted ultrasound frequency and sampling frequency of the received echoes were 7.5 and 40 MHz, respectively. The longitudinal cross-section of the phantom was measured with $M = 61$ ultrasonic beams. The beam spacing δx was 150 μm, and the frame rate was 187 Hz. As discussed in the results section, a rectangular window with a width of 0.48 mm (−6 dB cutoff spatial frequency: 1.22 mm^{-1}) was used for the HPF.

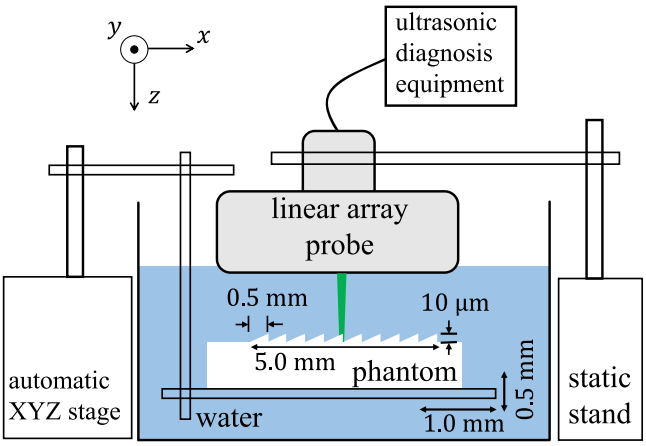

Fig. 5. (Color online) Schematic of the basic experiment using a silicone phantom.

2.5. In vivo experiments

Ultrasonic RF data were obtained for two heartbeats from the right common carotid arteries of two young and healthy volunteers, A (22 year old male, non-smoker) and B (23 year old male, non-smoker). The in vivo measurement in this study was approved by the Ethics Committee of the Graduate School of Engineering at Tohoku University (No. 19A-5). Both participants agreed to participate in the study. The ultrasound measurement conditions were the same as for the phantom experiment. The cutoff spatial frequency of the HPF is determined in the results section.

Based on the degree of coincidence among beams for roughness $\hat{r}_{\mathrm{HPF},m}(\xi)$ measured by each beam m using Eq. (15), the proposed method was compared with the previous method[19] which assumes that the axial displacement caused by pulsation is the same in all longitudinal positions. The root mean squared deviation (RMSD) of the roughness $\hat{r}_{\mathrm{HPF},m}(\xi)$ measured for each beam m [Eq. (15)] from the finally estimated roughness $\hat{r}_{\mathrm{HPF}}(\xi)$ [Eq. (16)] was obtained, and the averaged value SD_{r} for all beams was evaluated by the previous and proposed methods for each heartbeat and subject:

$$SD_{\mathrm{r}} = \frac{1}{M - 2W} \times \sum_{m=W}^{M-1-W} \sqrt{\frac{1}{\max x_{\mathrm{p}}(n) + 1} \sum_{\xi=x_m}^{x_m - \max x_{\mathrm{p}}(n)} |\hat{r}_{\mathrm{HPF},m}(\xi) - \hat{r}_{\mathrm{HPF}}(\xi)|^2}. \tag{19}$$

3. Results

3.1. Basic experiments using silicone phantom

Figure 6 shows the spatial frequency spectrum of the axial displacement $\widehat{\Delta d}(n; x_m)$ measured by the phased-tracking method[33–35] (blue line), which was averaged for all frames, the phantom surface roughness measured by the laser (red line), and the HPF (black line). The surface roughness

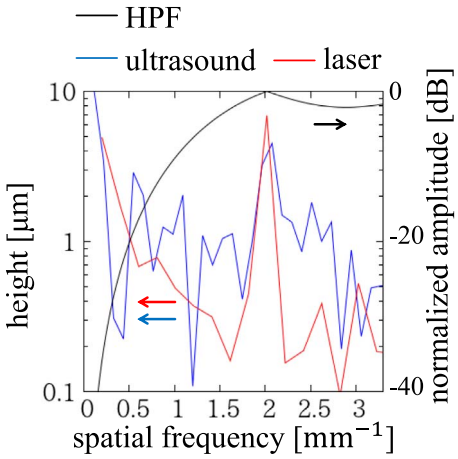

Fig. 6. (Color online) Spatial frequency spectra of the phantom surface profile measured by laser displacement meter (red line, right vertical axis) and ultrasound using the proposed method (blue line, right vertical axis), and spatial frequency characteristic of the HPF $g(x)$ (black line, left vertical axis) whose window width is $2W + 1 = 0.48$ mm (−6 dB cutoff frequency: 1.22 mm^{-1}).

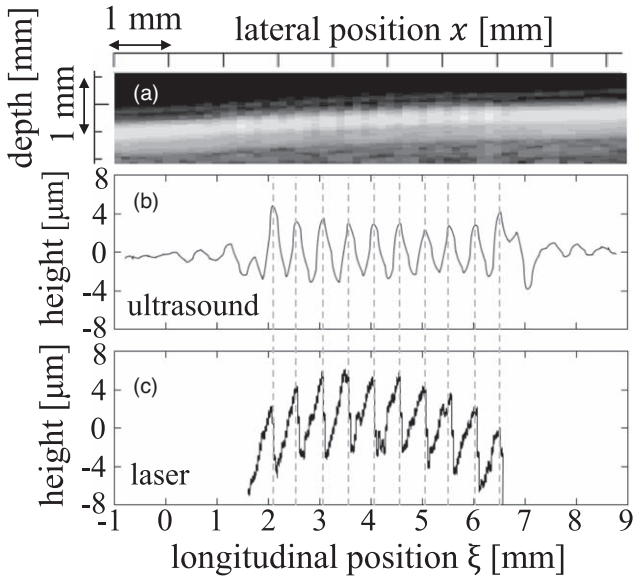

Fig. 7. Results of the phantom experiment. (a) B-mode image of the phantom surface, (b) estimated surface roughness $\hat{r}_{\mathrm{HPF}}(\xi)$ by the proposed method, and (c) surface roughness measured by the laser displacement meter.

measured by laser had approximately 7 μm height components at a spatial frequency of 2 mm^{-1}. The measured axial displacement $\widehat{\Delta d}(n; x_m)$ components were also observed around 2 mm^{-1} spatial frequency. Based on these spectra, a cutoff frequency for the HPF was set to 1.22 mm^{-1} such that the surface roughness components with the spatial frequency band of 2 mm^{-1} pass through, as shown by the black line in Fig. 6.

Figures 7(a)–7(c) show the B-mode image of the phantom surface, the estimated surface roughness $\hat{r}_{\mathrm{HPF}}(\xi)$ by the proposed method, and the surface roughness measured from the laser displacement meter, respectively. The longitudinal position of the measurement result from the laser displacement meter was adjusted to be that the top of the saw teeth aligned with that measured by the proposed method.

The difference of the height between the top and bottom of the saw teeth estimated by the proposed method was 4.91 ± 0.71 μm (average ± standard deviation for ten saw teeth), and the interval between adjacent bottoms was 481 ± 35 μm. From the results, the proposed method measured the surface profile with ten saw teeth, although the average height was 2.37 μm lower and the measured top edges of teeth were rounded compared with those measured by the laser.

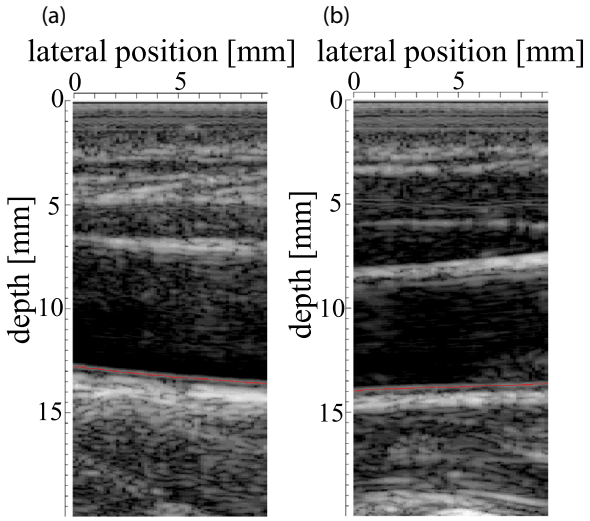

Fig. 8. (Color online) B-mode images of the right common carotid artery. (a) Subject A and (b) subject B. Red lines show the initially measured depths $\hat{z}(x_m; 0)$.

3.2. In vivo experiments

Figures 8(a) and 8(b) show B-mode images of the right common carotid artery for the two healthy young volunteers, A and B, respectively. The red line on the IMC represents the tracking depth $\hat{z}(x_m; 0)$ of the IMC determined by the thresholding.

Figure 9 shows the measured axial displacement $\hat{d}(n; x_m)$ for each beam m; these differ by up to 100 μm in the same frame [different colors in Fig. 9]. If IMC is inclined by the angle θ, the measured surface roughness, $r(\xi)$ relates to the true surface roughness $r_{\mathrm{t}}(\xi)$ as shown in Eq. (20)

$$r(\xi) = r_{\mathrm{t}}(\xi)\cos\theta. \tag{20}$$

In this study, the measurement range was 9.15 mm, and the value of cosθ is 0.9999. Therefore, the measured surface roughness and the true surface roughness are almost identical.

Figure 10 shows the spatial frequency spectra of the measured axial displacements $\widehat{\Delta d}(n; x_m)$, averaged for all frames. It has been reported that this roughness is caused by an increase in endothelial cells and damage to the internal elastic lamina.[8] Since there is no significant difference in cell size between humans and rabbits,[23,24] the height of the surface roughness in humans may be of the same order of ten micrometers as in rabbits. Thus, we set the −6 dB cutoff frequency of the HPF to 0.12 mm^{-1} ($2W + 1 = 1.5$ mm) as shown by the black line in Fig. 10, to pass through the higher frequency components that have approximately a height of 10 μm.

Figure 11(a) shows examples of the measured depths of IMC at different frames n, $\hat{z}(x_m; n = 84)$ (red line) and $\hat{z}(x_m; n = 112)$ (blue line). Although the lateral positions of $\hat{z}(x_m; n)$ were adjusted to the longitudinal positions ξ on the IMC by $\xi = x_m - x_{\mathrm{p}}(n)$, the measured depths do not correspond to each other even at the same longitudinal position ξ. The axial displacement caused the difference $d_{\mathrm{p}}(n; \xi)$ due to pulsation and/or height shift ΔD_m due to the regions of non-uniform sound-speed.

Figure 11(b) shows the surface profile $\hat{h}_m(\xi)$ for each beam m obtained by removing the axial displacement $d_{\mathrm{p}}(n; \xi)$ due to pulsation and the base depth D_0 from $\hat{z}(x_m; n)$ using the HPF by Eq. (8).

In Fig. 11(b), similar surface profiles were measured for each beam by applying the HPF [different colors in Fig. 11(b)], although there are offset-differences among surface profiles measured by different beams, that are caused by the height shift $\widehat{\Delta D}_{\mathrm{HPF},m}$ due to the region of non-uniform sound-speed, as shown in Fig. 3.

Figure 11(c) shows the surface roughness $\hat{r}_{\mathrm{HPF},m}(\xi)$ obtained by removing the height shift $\widehat{\Delta D}_{\mathrm{HPF},m}$ from $\hat{h}_{\mathrm{in},m}(\xi)$ by Eq. (15). By removing the height shift $\widehat{\Delta D}_{\mathrm{HPF},m}$ caused by the regions of non-uniform sound-speed, similar surface roughnesses were measured by each beam [different colors in Fig. 11(c)].

Figures 12(a) and 12(b) show the finally estimated surface roughnesses $\hat{r}_{\mathrm{HPF}}(\xi)$ by Eq. (16) for subjects A and B,

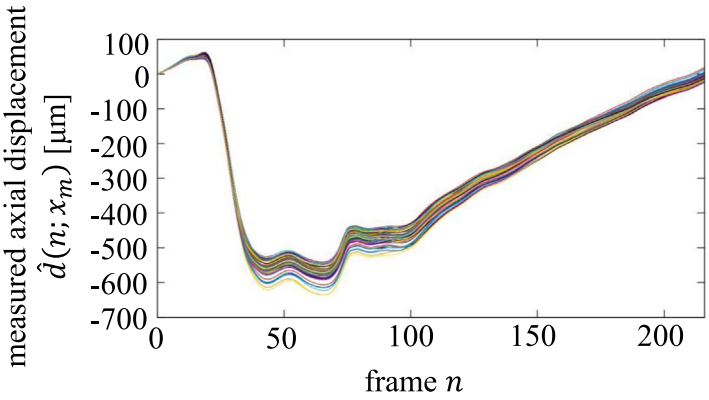

Fig. 9. (Color online) Measured axial displacement $\hat{d}(n; x_m)$ for each beam m.

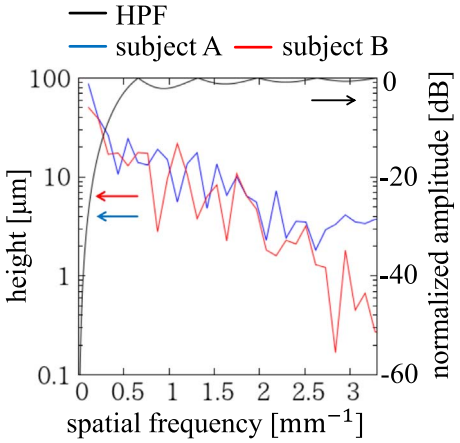

Fig. 10. (Color online) Averaged spectra of measured axial displacements $\hat{d}(n; x_m)$ for all frames (blue line: subject A, red line: subject B, right vertical axis), and spatial frequency characteristics of HPF (black line, left vertical axis) whose window width is $2W + 1 = 1.5$ mm (−6 dB cutoff frequency: 0.12 mm^{-1}).

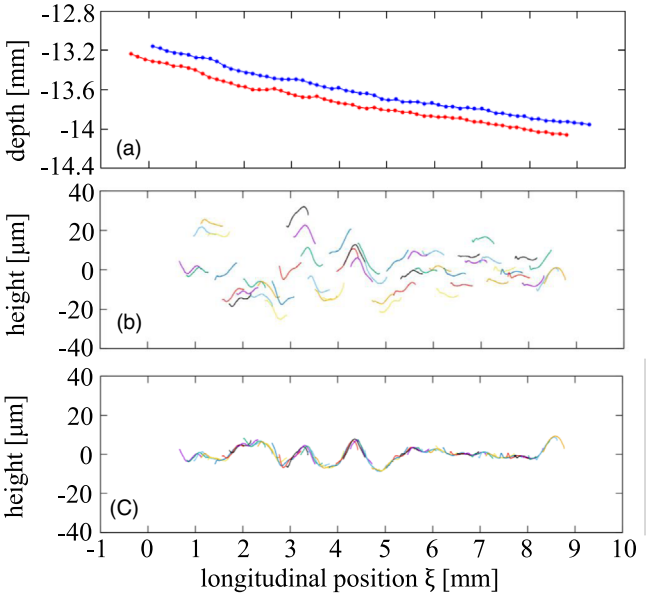

Fig. 11. (Color online) (a) Measured depths of the IMC at different frames n, $\hat{z}(x_m; 84)$ (red line) and $\hat{z}(x_m; 112)$ (blue line). (b) Surface profile $\hat{h}_{\mathrm{in},m}(\xi)$ measured for each beam m. (c) Surface roughnesses $\hat{r}_{\mathrm{HPF},m}(\xi)$ obtained by removing the height shift $\widehat{\Delta D}_{\mathrm{HPF},m}$ from $\hat{h}_{\mathrm{in},m}(\xi)$.

Table I. Root mean squared deviation $\mathrm{SD_r}$ of estimated roughness values. Specifically, the deviation between the estimated roughness $\hat{r}_{\mathrm{HPF},m}(\xi)$ obtained from each individual beam and the average roughness $\hat{r}_{\mathrm{HPF}}(\xi)$ overall beams are shown below.

	Previous method	Proposed method
Subject A (first beat)	0.63 μm	0.44 μm
Subject A (second beat)	0.51 μm	0.27 μm
Subject B (first beat)	0.45 μm	0.36 μm
Subject B (second beat)	0.53 μm	0.29 μm

respectively. The results for two consecutive heartbeats are overlaid. The surface roughness of approximately 10 μm height was estimated for both subjects, and the results for each heartbeat matched well.

Table I shows the averaged RMSD for all beams, SD_r, obtained by Eq. (19). The proposed method reduced the RMSD, that is, reduced the deviation of the measured surface roughness $\hat{r}_{\mathrm{HPF},m}(\xi)$ among beams, compared with the previous method[19] which assumes that the axial displacement caused by pulsation was the same in all longitudinal positions.

4. Discussion

In this paper, we propose a method to measure the minute surface roughness on the IMC of the carotid artery by removing the axial displacement caused by pulsation. The proposed method was validated by phantom and in vivo measurements.

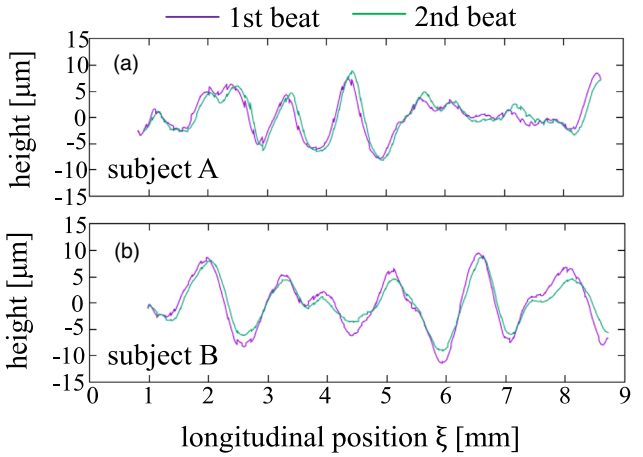

Fig. 12. (Color online) Finally estimated surface roughnesses $\hat{r}_{\mathrm{HPF}}(\xi)$ by the proposed method. (a) Subject A, (b) subject B (purple: 1st heartbeat, green: 2nd heartbeat).

The proposed method correctly measured the surface profile with ten saw teeth in the phantom experiment.

However, the height of the saw teeth measured by the proposed method was approximately 2.37 μm lower, and the measured top edges of the saw teeth were rounded compared with those measured by the laser. These results may be caused by the ultrasonic beam's lower spatial resolution in the lateral direction than the laser. Thus, there is a limitation caused by the ultrasound spatial resolution for the measurable spatial frequency of the surface roughness, as with the other ultrasonic measurement techniques.

In in vivo measurements, the cutoff frequency of the HPF to remove the axial displacement caused by pulsation was determined from the spatial frequency spectrum of the measured axial displacement based on the assumption that the height of surface roughness is approximately 10 μm because the actual spatial frequency characteristics of the surface roughness were unknown in in vivo. However, the cutoff frequency should be determined considering the actual spatial frequency characteristics of the surface roughness in our future study, which requires animal experiments, whose real surface roughness is measurable.

As shown in Table I, it was confirmed that the proposed method was superior to the previous method[19] which assumed that the axial displacement caused by pulsation was the same in all longitudinal positions.

5. Conclusion

In this paper, we propose an ultrasonic measurement method for the luminal surface roughness on the carotid artery wall by removing the axial displacement due to pulsation using the spatial HPF. The proposed method measured the surface roughness in tens of micrometers in the basic experiment using the phantom. In in vivo measurements involving two healthy subjects, the variation in measured surface roughness among beams was reduced by the proposed method, and reproducible results were obtained for consecutive heartbeats.

Acknowledgments

The part of this work was supported in part by JSPS KAKENHI 19KK0100 and 21H03835.

1) K. J. Foreman et al., Lancet **392**, 2052 (2018).
2) S. J. Nicholls et al., J. Am. Coll. Cardiol. **47**, 1967 (2006).
3) J. C. Bramwell and A. V. Hill, Proc. R. Soc. B **93**, 298 (1922).
4) J. C. Bramwell, A. V. Hill, and B. A. McSwiney, Heart **10**, 233 (1923).
5) P. Hallock, Arch. Int. Med. **54**, 770 (1934).
6) T. Yamagishi, M. Kato, Y. Koiwa, H. Hasegawa, and H. Kanai, J. Atheroscler. Thromb. **16**, 782 (2009).
7) M. W. Lorenz, H. S. Markus, M. L. Bots, M. Rosvall, and M. Sitzer, Circulation **115**, 459 (2007).
8) E. Sho, M. Sho, T. M. Singh, H. Nanjo, M. Komatsu, C. Xu, H. Masuda, and C. K. Zarins, Exp. Mol. Pathol. **73**, 142 (2002).
9) R. Ross and J. A. Glomset, Science **180**, 1332 (1973).
10) R. Ross, N. Engl. J. Med. **340**, 115 (1999).
11) A. Schmidt-Trucksäss, M. Sandrock, D.-C. Cheng, H.-M. Müller, M. W. Baumstark, R. Rauramaa, A. Berg, and M. Huonker, Atherosclerosis **166**, 57 (2003).
12) M. Sandrock, C. Schulze, D. Schmitz, H.-H. Dickhuth, and A. Schmidt-Trucksaess, Br. J. Sports Med. **42**, 839 (2008).
13) A. Krebs, A. Schmidt-Trucksäss, J. Wagner, K. Krebs, J. Doerfer, and K. O. Schwab, Pediatr. Diabetes **6**, 161 (2005).
14) R. Nagaoka, J. E. Wilhjelm, and H. Hasegawa, J. Med. Ultrason. **47**, 493 (2020).
15) K. Nagata, R. Nagaoka, J. E. Wilhjelm, and H. Hasegawa, Jpn. J. Appl. Phys. **60**, SDDE09 (2021).
16) C. Arihara, H. Hasegawa, and H. Kanai, Jpn. J. Appl. Phys. **45**, 4727 (2006).
17) M. Cinthio, H. Hasegawa, and H. Kanai, Proc. IEEE Ultrason. Symp., 2007, p. 997.
18) M. Cinthio, H. Hasegawa, and H. Kanai, IEEE Trans. Ultrason. Ferroelectr. Freq. Control **58**, 853 (2011).
19) K. Kitamura, H. Hasegawa, and H. Kanai, Jpn. J. Appl. Phys. **51**, 07GF08 (2012).
20) Y. Nagai, M. Cinthio, H. Hasegawa, M. Bengtsson, M. Evander, J. Albinsson, and H. Kanai, J. Med. Ultrason. **41**, 431 (2014).
21) Y. Nagai, H. Hasegawa, and H. Kanai, Jpn. J. Appl. Phys. **53**, 07KF19 (2014).
22) S. Mori, T. Abe, M. Arakawa, J. E. Wilhjelm, and H. Kanai, Proc. IEEE Ultrason. Symp., 2020, 10.1109/IUS46767.2020.9251812.
23) M. Félétou, *The Endothelium* (Morgan and Claypool Life Sciences, San Rafael, CA, 2011), Chap. 1.
24) M. J. Legg and B. S. Gow, Atherosclerosis **39**, 277 (1981).
25) J. K.-J. Li, J. Melbin, R. A. Riffle, and A. Noordergraaf, Circ. Res. **49**, 442 (1981).
26) J. K.-J. Li, J. Melbin, K. Campbell, and A. Noordergraaf, J. Biomech. **13**, 1023 (1980).
27) W. R. Milnor and W. W. Nichols, Circ. Res. **36**, 631 (1975).
28) W. R. Milnor and C. D. Bertram, Circ. Res. **43**, 870 (1978).
29) R. Yamane, S. Mori, M. Arakawa, J. E. Wilhjelm, and H. Kanai, Proc. Symp. Ultrason. Electron. **43**, 403 (2022).
30) S. Golemati, A. Sassano, M. J. Lever, A. A. Bharath, S. Dhanjil, and A. N. Nicolaides, Ultrasound Med. Biol. **29**, 387 (2003).
31) J. H. Velduis and G. W. Brodland, Image Vis. Comput. **17**, 905 (1999).
32) I. Céspedes, Y. Huang, J. Ophir, and S. Spratt, Ultrason. Imaging **17**, 142 (1995).
33) H. Kanai, Y. Koiwa, and J. Zhang, IEEE Trans. Ultrason. Ferroelectr. Freq. Control **46**, 1229 (1999).
34) H. Kanai, M. Sato, Y. Koiwa, and N. Chubachi, IEEE Trans. Ultrason. Ferroelectr. Freq. Control **43**, 791 (1996).
35) H. Kanai, K. Sugimura, Y. Koiwa, and Y. Tsukahara, Electron. Lett. **35**, 949 (1999).
36) M. Ito, M. Arakawa, and H. Kanai, Jpn. J. Appl. Phys. **57**, 07LF14 (2018).

